Monthly Notices of the ROYAL ASTRONOMICAL SOCIETY

MNRAS **518,** 4930–4942 (2023) https://doi.org/10.1093/mnras/stac3352
Advance Access publication 2022 November 17

Intensification of magnetic field in merging magnetic flux tubes driven by supergranular vortical flows

Abraham C.-L. Chian,[1,2]★ Erico L. Rempel,[2,3] Suzana S. A. Silva,[4] Luis Bellot Rubio[5] and Milan Gošić[6,7]

[1]*School of Mathematical Sciences, University of Adelaide, Adelaide, SA 5005, Australia*
[2]*National Institute for Space Research (INPE), P.O. Box 515, São José dos Campos, São Paulo 12227-010, Brazil*
[3]*Aeronautics Institute of Technology (ITA), São José dos Campos, São Paulo 12228-900, Brazil*
[4]*Plasma Dynamics Group, Department of Automatic Control and Systems Engineering, University of Sheffield, Sheffield S1 3JD, UK*
[5]*Instituto de Astrofísica de Andalucía (IAA-CSIC), Apartado de Correos 3004, E-18080 Granada, Spain*
[6]*Lockheed Martin Solar and Astrophysics Laboratory, Palo Alto, CA 94304, USA*
[7]*Bay Area Environmental Research Institute, Moffett Field, CA 94035, USA*

Accepted 2022 November 14. Received 2022 November 9; in original form 2022 September 2

ABSTRACT

The spatiotemporal dynamics of vorticity and magnetic field in the region of a photospheric vortex at a supergranular junction of the quiet Sun is studied, using *Hinode*'s continuum intensity images and longitudinal magnetograms. We show that in a 30-min interval during the vortex lifetime, the magnetic field is intensified at the centres of two merging magnetic flux tubes trapped inside the vortex boundary. Moreover, we show that the electric current density is intensified at the interface boundary layers of merging tubes, resulting from strong vortical downflows in a supergranular vertex. Evidence of Lagrangian chaos and vortex stretching in the photospheric plasma turbulence responsible for driving the intensification of magnetic fields is analysed. In particular, we report the first solar observation of the intensification of electromagnetic energy flux resulting from the merger of magnetic flux tubes.

Key words: chaos – turbulence – Sun: granulation – Sun: magnetic fields – Sun: photosphere.

1 INTRODUCTION

The solar network (NE) magnetic fields are among the most distinct structures of the photosphere. They outline the supergranular junctions in the quiet and active Sun, where the diverging flows from nearby supergranular cells collide and turn into converging downdrafts with strong shear where cold plasma returns to the solar interior, leading to complex interactions between turbulent convective flows and magnetic fields. The network magnetic fields are organized into predominantly vertical kilogauss (kG) flux tubes and form patches of intense magnetic flux concentrations that can persist for hours and even days (Bellot Rubio & Orozco Suárez 2019). Bale et al. (2021) proposed that magnetic switchbacks observed by *Parker Solar Probe* in the near-Sun solar wind are driven by interchange magnetic reconnection events, with the footpoints of merging closed and open magnetic flux ropes rooted at supergranular junctions, just above the solar transition region and the spacecraft measurements represent the extended regions of a turbulent outflow of magnetic reconnection exhaust. Fargette et al. (2021) concluded that switchbacks are formed in the low corona and modulated by the solar surface convection patterns of supergranulation and granulation; the large scales detected for switchback patches are compatible with supergranulation scales and the smaller scales are compatible with granulation scales.

Vorticity plays an important role in the evolution of network magnetic fields. The first evidence of a persistent photospheric vortex with lifetime of over 1.5 h was reported by Brandt et al. (1988) using the *Swedish Solar Telescope (SST)*. They observed a vortex with a diameter of around 5 Mm located at a supergranular boundary and dominates the dynamics of a group of granules in its vicinity, which spiral around and disappear in the vortex centre. Some granules are elongated along the velocity streamlines and compressed perpendicular to the streamlines. They suggested that vortical motions can twist magnetic fields and induce electric currents at the footpoints of magnetic flux tubes, providing a mechanism for chromospheric-coronal heating. Attie, Innes & Potts (2009) detected two persistent vortices at supergranular junctions with lifetimes over 1 and 2 h, respectively, using *Hinode* continuum images of the quiet Sun. They showed an example of a magnetic element of negative polarity rotating clockwise around a magnetic element of positive polarity advected by the vortical motion. Innes et al. (2009) observed microflares and mini-coronal mass ejections at supergranular junctions in the quiet Sun in association with brightenings seen on *STEREO* EUV images. These activities are activated by converging vortical photospheric flows which appear to twist small concentrations of mixed-polarity magnetic fields in shear flow regions (Silva et al. 2020).

Vertically oriented rotating magnetic flux tubes with lifetimes over 40 min were detected by Balmaceda et al. (2010) using *Hinode* and *SST*. The rotation of magnetic structures led to fragmentation

★ E-mail: abraham.chian@gmail.com

and coalescence of magnetic bright points along the intergranular lane. They saw magnetic concentrations being dragged towards the centre of a persistent vortex with lifetime over 20 min. After the disappearance of the vortex, the magnetic flux tube continues its movement with decreasing velocity towards a new sink, perhaps affected by the adjacent granules. Yang et al. (2015) used *SDO*/HMI line-of-sight magnetic field images and AIA UV/EUV images to study a rotating magnetic field structure driven by a persistent vortex located at the quiet-Sun supergranular junctions where the footpoint of a circular filament is anchored. The rotation of the NE vortex and magnetic structures enables the build-up of magnetic free energy and helicity in the filament and its eruption. Attie et al. (2016) used photospheric and X-ray data from *SoHO* and *Hinode* to analyse micro-flares at several sites of converging opposite-polarity magnetic fluxes at supergranular junctions in the quiet Sun, sometimes linked to observable vortex-like motion. They concluded that X-ray network flares occur at sites of magnetic energy dissipation and attributed the magnetic energy amplification of NE micro-flares to supergranular vortical flows that cause systematic shearing of the magnetic field.

Magnetic bright points associated with kG magnetic flux tubes are ubiquitous in the quiet and active solar photosphere–chromosphere, which are located at supergranular junctions and intergranular lanes. Observations and numerical simulations have identified a wealth of physical processes that can contribute to rapid intensification of magnetic field strength of magnetic bright points, including convective collapse, granular compression, merging, and vorticity (Keys et al. 2020). An example of fast magnetic field amplification in the Sun, in a time interval of ∼30–100 s, was shown by Keys et al. (2020) based on a MURaM simulation when a magnetic bright point (MBP) moves into a region of higher vorticity. However, they did not see this phenomenon in their ground-based observations of magnetic bright points, thus demonstrating the need to improve the techniques of observing the vorticity-magnetic field relation. The formation process of kG magnetic flux tubes starts with the advection of magnetic fields by horizontal convective flows to the downflow regions. This process known as flux expulsion allows the field strength to build up to the limit roughly given by the equipartition of the magnetic energy density of magnetic flux tubes and the kinetic energy density of the granular flows. Convective instability then provides further intensification to kG field strength by causing the plasma in magnetic flux tubes to cool, evacuate, and narrow until the field strength is sufficiently strong to suppress the instability (Parker 1978). The intensified field strength is given by the balance between the magnetic pressure of the evacuated magnetic flux tube and the surrounding gas pressure. This process known as convective collapse (Spruit 1979) has been confirmed by observations (Bellot Rubio et al. 2001; Nagata et al. 2008; Vargas Domínguez et al. 2015; Keys et al. 2020) and numerical simulations (Hewitt et al. 2014; Kitiashvili et al. 2015; Keys et al. 2020). Magnetic field intensification due to granular compression has been detected by MURaM radiative MHD simulations and ground-based observations of MBPs using *SST* in the quiet-Sun's disc centre based on automated feature-tracking algorithms (Keys et al. 2020). When the granules on both sides of an MBP expand they exert a pressure force to compress the MBP, resulting in its stretching along the intergranular lane and the magnetic field intensification; the elongated MBP splits when they are squeezed between two moving granules (Requerey et al. 2015).

An accurate description of vorticity in fluids and plasmas requires the vortices to be objective, i.e. remain unchanged under time-dependent rotations and translations of the coordinate frame. Haller et al. (2016) proposed a technique to detect an objective vortex with guaranteed material invariance and experimentally observable rotational coherence, which defines an objective Lagrangian vortex for a finite-time interval as a set of tubular surfaces, each exhibiting uniform intrinsic rotation rate; such vortex tube is foliated by outward-decreasing tubular level surfaces of the Lagrangian-averaged vorticity deviation (LAVD). In the limit of zero advection time, an objective Eulerian (instantaneous) vortex is defined as a set of tubular surfaces of equal intrinsic rotation rate; such vortex tube is foliated by outward-decreasing tubular level surfaces of the instantaneous vorticity deviation (IVD). The vortex boundary on a plane section is given by the outermost convex closed contour of the LAVD or IVD scalar field around the vortex centre, which in turn is defined by a local maximum of the LAVD or IVD field. The computing of LAVD and IVD requires the choice of a convexity deficiency parameter given by the maximum amount of deviation from convexity a curve may have to describe a vortex. Integrated-averaged current deviation (IACD) and local current deviation (LCD) have been adapted from LAVD and IVD by Rempel et al. (2017) to detect objective magnetic vortices. A number of papers have applied LAVD/IVD and IACD/LCD to detect kinematic (i.e. velocity) and magnetic vortices in solar plasmas (Rempel et al. 2017; Silva et al. 2018, 2020, 2021, 2022; Chian et al. 2019, 2020).

Kitiashvili et al. (2012) simulated the formation and dynamics of small-scale vortex tubes driven by turbulent magnetoconvection in the quiet Sun; these vortex tubes are mostly concentrated in intergranular lanes characterized by strong helical downflows and swirling motions that capture, stretch, and twist magnetic field lines, resulting in the formation of magnetic flux tubes expanding with atmospheric height, which can account for the origin of the myriad of small-scale open and closed magnetic loops that cover the solar surface (Gošić et al. 2022). The magnetic energy grows mostly at the edge of granules (i.e. intergranular lanes) and at the periphery of turbulent vortex tubes, where shear motions are strongest. The ubiquitous magnetized vortex tubes in subsurface layers may generate electric currents and lead to eruptions, such as high-speed jets (e.g. spicules) that transfer mass and energy into solar corona and may even feed the solar wind (Kitiashvili et al. 2013). Those electric currents show a clear correlation with the swirling dynamics of convective flows. The strongest electric current density is found at the periphery of helical motions (Silva et al. 2021), or in the space between vortices, where stretching of the magnetic field lines is the strongest. Candelaresi et al. (2018) applied MHD simulation of magnetoconvection and *Hinode* observations of an active region plage to obtain evidence of twisting or braiding of entangled coronal magnetic field lines driven by photospheric vortical motions. Martínez-Sykora et al. (2019) simulated the impact of internetwork quiet-Sun photosphere on the chromosphere and detected a mechanism of converting kinetic energy into magnetic energy in the lower chromosphere involving stretch-twist-fold and reconnection of magnetic fields, when the chromosphere is dominated by magnetized shocks. Silva et al. (2020) applied the IVD to detect 3D intergranular objective kinematic vortices using MURaM code, which showed that kinematic vortices intensify the magnetic field at the sinking points of plasma downflows and the magnetic field in turn plays a fundamental role in the evolution of kinematic vortices. In general, kinematic vortices do not give rise to magnetic vortices unless their tangential velocities at different height levels are high enough to overcome the magnetic tension (Silva et al. 2021). The objective kinematic vortices are located between regions of intense electric current density and tend to appear in the low-pressure regions. The magnetic field lines are mostly vertically oriented and organized into tubular structures. Silva et al. (2021) applied the IACD to detect 3D intergranular objective magnetic vortices using MURaM code,

which show that objective magnetic vortices are found mostly in the plasma-$\beta > 1$ region whereas objective kinematic vortices are found in the plasma-$\beta < 1$ region.

Poynting flux is the primary mechanism for transport of electromagnetic energy in the solar atmosphere. Shelyag, Mathioudakis & Keenan (2012) found in a numerical simulation of solar plage that the horizontal motions of solar photospheric vortices act as the primary source of vertical Poynting flux. In addition to generating an upward-pointing Poynting flux, small-scale vortices in the photosphere can provide electromagnetic energy to heat the chromosphere (Yadav, Cameron & Solanki 2020). In a recent Bifrost numerical simulation of the quiet-Sun atmosphere, Silva et al. (2022) found out that the total electromagnetic energy flux in the photosphere occurs mainly parallel to the horizontal plane of the photosphere, concentrating in localized regions along the intergranular lanes. This result was validated by the *SUNRISE/IMaX* data. The dominance of the horizontal component of the electromagnetic energy flux is observed in the photosphere as well as in some atmospheric layers, especially in regions with a strong concentration of electromagnetic energy and where the magnetic field is predominantly vertical. When the swirling motions perturb the magnetic field lines in the upper photosphere and chromosphere, a net upward Poynting flux can be generated (Shelyag et al. 2012; Yadav et al. 2020; Battaglia et al. 2021).

The aim of this paper is to study the relation between vorticity and magnetic field in the supergranular turbulence by investigating the intensification of magnetic field and electromagnetic energy flux at the centres of two merging magnetic flux tubes and the intensification of electric current densities at their interface boundary layers driven by a persistent objective kinematic vortex at a supergranular vertex of the quiet-Sun's disc centre.

In Section 2, we analyse the spatiotemporal dynamics of *Hinode*'s line-of-sight magnetic field, horizontal velocity field, and horizontal electric current density derived from the line-of-sight magnetic field, and compute the local current deviation in the supergranular region of a persistent objective kinematic vortex detected by the instantaneous vorticity deviation. In Section 3, we study the spatiotemporal dynamics of the horizontal electric current density, the temporal growth of the maxima of line-of-sight magnetic fields at the centres of two merging magnetic flux tubes trapped in the interior of the vortex boundary, and the temporal growth of the maxima of the LCD at the interface boundary layers of two merging magnetic flux tubes. In Section 4, we present the observational evidence of stretching-twisting-folding in the Lagrangian chaotic spatiotemporal dynamics of turbulent vortical flows. In Section 5, we use the computed horizontal electromagnetic energy flux to investigate the temporal growth of core electromagnetic energy fluxes in the merging magnetic flux tubes. In Section 6, we discuss the physical mechanisms responsible for the intensification of magnetic fields, electric current densities, and electromagnetic energy fluxes in multiple magnetic flux tubes undergoing merging trapped by supergranular vortical flows.

2 MAGNETIC FIELD AND ELECTRIC CURRENT DENSITY IN SUPERGRANULAR VORTICAL FLOWS

Chian et al. (2020) investigated the genesis and life cycle of persistent objective kinematic vortices at supergranular junctions in the quiet Sun using *Hinode* spacecraft imaging of the photosphere. Their analysis was carried out using the photospheric horizontal velocity fields derived by the local correlation tracking (LCT) method from an ≈22 h sequence of *Hinode* continuum intensity images of the Sun's disc centre, with a cadence of 90 s, from 08:31:15 UT on 2010 November 2 to 06:19:42 UT on 2010 November 3. The intensity maps, longitudinal magnetograms, and Dopplergrams were construted from the observed Stokes I and V images (Gošić et al. 2014). To test the quality of the velocity data, the LCT method was applied to the *Hinode* continuum intensity images and Dopplergrams using a tracking window with an Full Width at Half Maximum (FWHM) = 2.9 Mm that was averaged over the whole time sequence of 24 h, and it was confirmed that the mean horizontal velocity fields given by the continuum intensity images and the Dopplergrams are almost the same. In this paper, we will analyse supergranular turbulent flows using time sequences of continuum intensity images with a 2-h time average (Requerey et al. 2018). Persistent (long-duration) vortices have been studied in this same supergranular region in a series of papers by Requerey et al. (2018), Silva et al. (2018), Chian et al. (2019, 2020), and Roudier et al. (2021). A set of 29 persistent objective kinematic vortices with lifetimes varying from 28.5 to 298.3 min were detected by Chian et al. (2020) at the boundary of a supergranular cell by computing the LAVD and the IVD. Within this set, a sequence of seven recurrent persistent objective kinematic vortices were found in a mixed-polarity magnetic region of a supergranular vertex. They are dominated by vortical downflows due to strong shears resulting from the interaction of converging flows from several nearby supergranular cells. In this paper, our study will be centred on one specific vortex of this sequence which appeared at 11:23:49 UT and disappeared at 14:23:53 UT on 2010 November 2, with a lifetime of ∼180 min, an initial IVD of 8.67×10^{-5}, a peak LAVD of 1.08, and a total LAVD of 942.46 during the vortex lifetime (corresponding to vortex B2 in fig. 2 and table 1 in Chian et al. 2020). Yadav et al. (2020) and Yadav, Cameron & Solanki (2021) identified vortical flows at various spatial scales in their MURaM simulation of a unipolar solar plage region for different effective spatial resolutions and concluded that the observed large vortices are likely clusters of much smaller vortices that are not yet resolved by observations. Hence, a vortex detected by the technique of LAVD and IVD may *de facto* consist of a number of smaller vortices.

The relation between a recurrent photospheric vortical flow and the evolution of a network magnetic element at a supergranular vertex for the same *Hinode* data set to be studied in this paper has been analysed previously by Requerey et al. (2018) for a long duration of 24 h. Their analysis showed that during the whole 24 h time series the vortical flows at the supergranular vertex consist of three recurrent vortices that appear almost at the same location. At the core of these vortices, a network magnetic element is also observed whose spatiotemporal behaviour is closely correlated to that of the vortices, namely, the magnetic feature is concentrated and evacuated when it is caught by the vortices and is weakened and fragmented after the vortical flows disappear. The study of Requerey et al. (2018) was done based on techniques that are not objective. In this paper, we will adopt objective techniques to improve the investigation of the relation between vorticity and magnetic field in supergranular turbulence. After carrying out a detailed survey in the lifetime of several long-duration objective vortices detected by Chian et al. (2020), we have selected an interval of 30 min of a vortex to depict clearly the vorticity-magnetic field relation using objective techniques. The analysed time interval corresponds to the peak of the vortex life, i.e. after the vortex is well developed and its effects on plasma dynamics have already begun to take place and before the vortex decaying process starts. This allows us to study properly the vortical impact on plasma dynamics since the vortex has reached its peak strength. Although we will focus our analysis for this 30-min interval in this paper, the methodology developed in this paper can be readily applied to study other time intervals of the whole time series.

Table 1. Temporal evolution of the area of a persistent objective kinematic vortex at the supergranular junction for the interval from frame 175 to frame 195 on 2010 November 2, providing observational signature of chaotic stretching evidenced by a steady vortical expansion.

Frame number	175	179	183	187	191	195
Time in UT	12:53:51	12:59:51	13:05:51	13:11:51	13:17:51	13:23:51
Vortex area in cm^2	4.619×10^{16}	7.083×10^{16}	1.112×10^{17}	1.484×10^{17}	1.506×10^{17}	1.531×10^{17}

In this paper, we will study the spatiotemporal dynamics of the line-of-sight magnetic field in the region of a persistent objective kinematic vortex in the photosphere detected by Chian et al. (2020), corresponding to the final interval of vortex-1 in figs 2–3 of Requerey et al. (2018). The objective kinematic vortex is identified by computing the IVD of a particle at a given position $\mathbf{x}$,

$$\mathrm{IVD}(\mathbf{x}, t) := |\omega(\mathbf{x}, t) - \langle\omega(t)\rangle|\,, \tag{1}$$

which is the integrand of the LAVD (Haller et al. 2016),

$$\mathrm{LAVD}_{t_0}^{t_0+\tau}(\mathbf{x}_0) := \int_{t_0}^{t_0+\tau} |\omega(\mathbf{x}(t), t) - \langle\omega(t)\rangle|\,dt, \tag{2}$$

where the vorticity $\omega = \nabla \times \mathbf{u}$, $\mathbf{u}$ is the velocity field, $<\omega(t)>$ is the instantaneous spatial mean of ω in the domain and $\mathbf{x}$ is the solution of $\dot{\mathbf{x}} = \mathbf{u}(\mathbf{x}(t), t)$, with $\mathbf{x}(t_0) = \mathbf{x}_0$. Note that the vorticity is not objective, i.e. frame-invariant, but the IVD and the LAVD are objective (Haller et al. 2016; Rempel et al. 2017). We will focus on an interval of 30 min during the lifetime of this vortex with counter-clockwise flows, from frame 175 to 195 (the corresponding time in UT is given in Table 1) on 2010 November 2. Fig. 1 shows the vortex boundary computed by the IVD method for 6 instants separated by 6 min, superposed by the line-of-sight magnetic field and the Line Integral Convolution (LIC) map of the horizontal photospheric velocity field calculated by Paraview using interpolated data. For the sake of consistency, we have fixed the value of convexity deficiency (Haller et al. 2016; Rempel et al. 2017) to 0.05 for all 6 instants to quantitatively monitor the spatiotemporal dynamics of the vortex.

Rempel et al. (2017,2019) proposed an adaptation of the LAVD operator for the magnetic field by considering a parametrization of a magnetic field line at time t_0 given by $\mathbf{x}(s)$, where s is a parameter related to the distance l along the field line by $dl = |\mathbf{B}|ds$. Then, the equation of a magnetic field line at a given time t_0 is given by

$$\frac{d\mathbf{x}}{ds} = \mathbf{B}(\mathbf{x}(s), t_0), \quad \mathbf{x}(s_0) = \mathbf{x}_0. \tag{3}$$

The IACD field can be computed for $\mathbf{B}$ in essentially the same way as LAVD is for the particle velocity $\mathbf{u}$, by using $\mathbf{J} = c\nabla \times \mathbf{B}/(4\pi)$ in lieu of $\omega = \nabla \times \mathbf{u}$:

$$\mathrm{IACD}_{s_0}^{s_0+\xi}(\mathbf{x}, t_0) := \int_{s_0}^{s_0+\xi} |\mathbf{J}(\mathbf{x}(s), t_0) - \langle\mathbf{J}(t_0)\rangle|\,ds, \tag{4}$$

where $\mathbf{x}(s)$ is a solution of equation (3) and $\langle\mathbf{J}(t_0)\rangle$ is the mean electric current density of the domain at t_0. Note that, different from LAVD, here the calculations are done for a fixed time t_0, since the magnetic field line equation, equation (3), is defined for a fixed time. The LCD is given by the integrand of equation (4)

$$\mathrm{LCD}(\mathbf{x}, t_0) := |\mathbf{J}(\mathbf{x}, t_0) - \langle\mathbf{J}(t_0)\rangle|\,. \tag{5}$$

Rempel et al. (2019) proved that IACD and LCD are objective quantities that are invariant under time-dependent translations and rotations of the reference frame, and pointed out that the detection of vortices using non-objective methods may lead to inconsistent results.

By assuming vertically oriented magnetic fields, which is a reasonable hypothesis for the footpoints of open and closed coronal loops (magnetic flux tubes) rooted at supergranular junctions, the horizontal electric current density (J_x, J_y) in the photosphere can be derived from the observed line-of-sight magnetic field by using the Ampere's law and neglecting the displacement current

$$J_x = \frac{c}{4\pi}\frac{\partial B_z}{\partial y}, \quad J_y = -\frac{c}{4\pi}\frac{\partial B_z}{\partial x}, \tag{6}$$

where B_z is the line-of-sight component of the magnetic field and c is the speed of light. In contrast to the work of Giannattasio et al. (2020), which studied the horizontal electric current density averaged on supergranular spatial and temporal scales, in this paper we are interested in the instantaneous dynamics of the horizontal electric current density. Fig. 2 shows the computed LCD for the same 6 instants of Fig. 1 in the region of supergranular turbulent flows, superposed by the vortex boundary computed by IVD and the LIC-map of the horizontal photospheric velocity field. During this time interval of 30 min, a steady expansion of the boundary layers occurs owing to vortical stretching that transforms a ring-shaped boundary layer encircling mainly the upper magnetic flux tube (a) to an elongated ellipse encircling the two merging magnetic flux tubes (f).

3 INTENSIFICATION OF MAGNETIC FIELD AND ELECTRIC CURRENT DENSITY

Fig. 3 shows the line-of-sight magnetic field superposed by the LIC-maps of the horizontal electric current density and the same vortex boundaries of Figs 1–2. It is worth mentioning that this figure was plotted using interpolated data that increased the resolution by four folds. The magenta square marks the location of the maximum of the line-of-sight magnetic field $B_{\max}$ numerically determined in the entire region of vortical flows of Fig. 3 for each instant. Note that $B_{\max}$ is located near the centre of the upper magnetic flux tube trapped in the interior of the persistent objective vortex detected by IVD. A MURaM simulation study of solar plage region by Silva et al. (2020) found that the centre of the intergranular vortices detected by IVD exhibits the largest value of magnetic field.

Fig. 4 shows the LCD computed by equation (5), superposed by the LIC-maps of the horizontal electric current density and the vortex boundaries of Figs 1-3. The orange square marks the location of the maximum of the $\mathrm{LCD}_{\max}$, numerically determined in the entire region of vortical flows of Fig. 4 for each instant. Note that $\mathrm{LCD}_{\max}$ is located at the interface boundary layers identified by the banded region of strong horizontal electric current density separating upper and lower magnetic flux tubes in Figs 2 and 4. An enlarged view of the interaction region of two merging magnetic flux tubes of Fig. 4(e) is shown in Fig. 5. The horizontal electric current density computed by equation (6) demonstrates that the magnetic element associated with a strong concentration of magnetic flux co-spatial with the centre of the supergranular vortical flow seen in Fig. 1(e) actually consists of two merging magnetic flux tubes marked by two arrows, which display low values of the horizontal electric current density at the tube centres due to our assumption of vertically oriented magnetic fields. The boundary layers of the merging magnetic flux

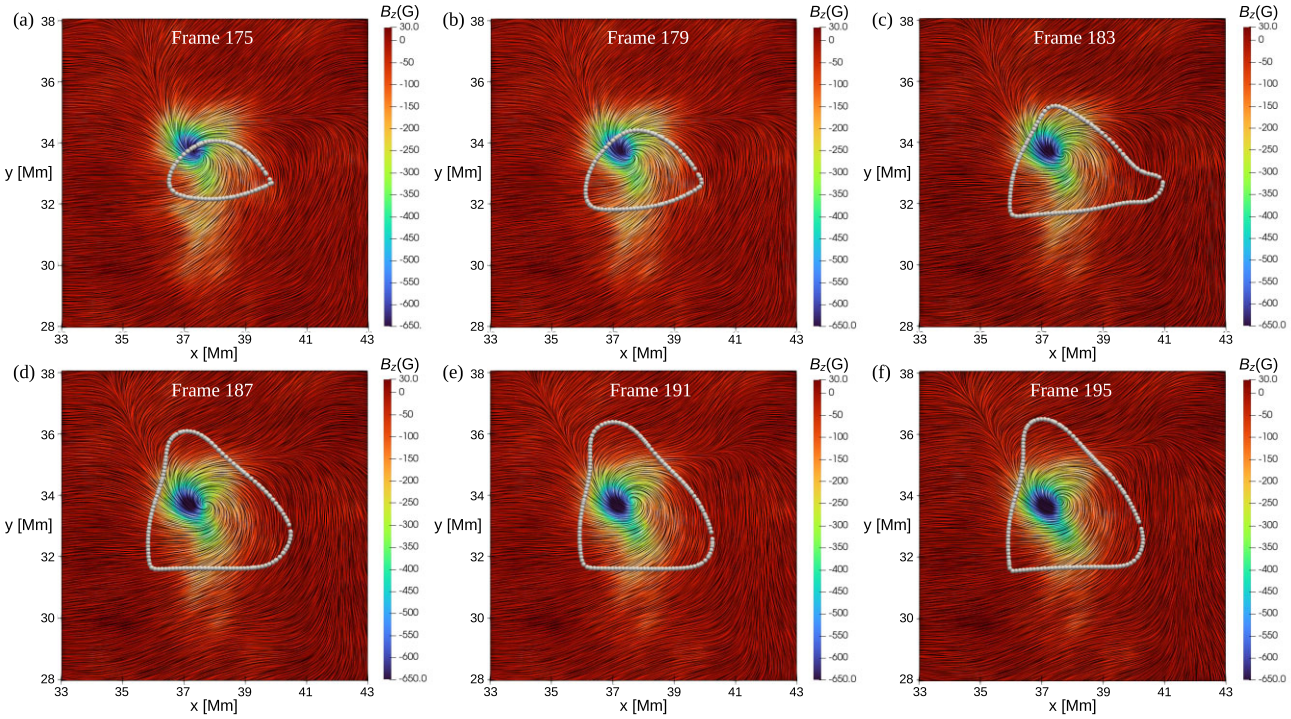

Figure 1. Spatiotemporal dynamics of a persistent objective kinematic vortex and line-of-sight magnetic field. *Hinode* observation of the LIC-maps of the horizontal photospheric velocity fields superposed by the boundary (gray circles) of the persistent objective kinematic vortex computed by the IVD by fixing the value of the convexity deficiency parameter to 0.05, and the line-of-sight magnetic field at a supergranular junction of the quiet-Sun's disc centre from frame 175 to 195 on 2010 November 2. For the sake of consistency, we will adopt the same value for the convexity deficiency parameter throughout this paper. The magnetic flux concentration is located adjacent to the converging centre of turbulent counter-clockwise vortical flows.

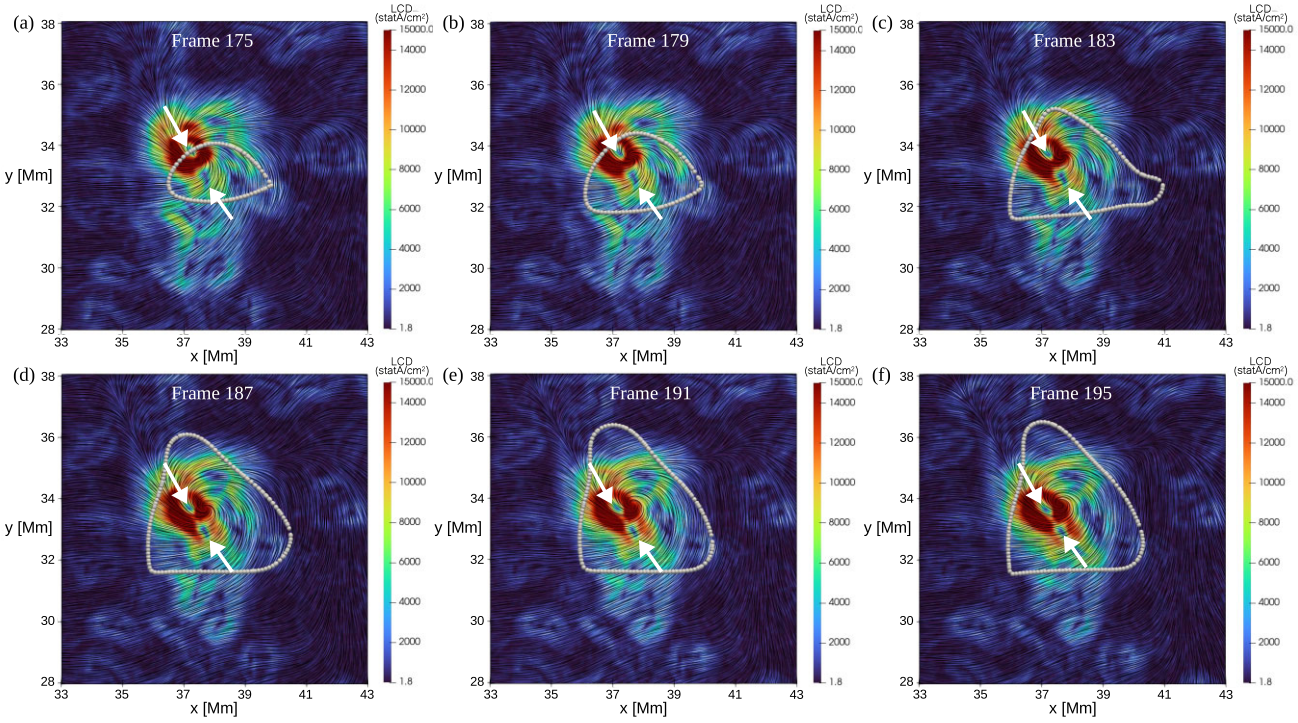

Figure 2. Spatiotemporal dynamics of a persistent objective kinematic vortex and LCD. The LIC-maps of the horizontal photospheric velocity fields superposed by the boundary (grey circles) of the persistent objective kinematic vortex computed by the IVD by fixing the value of convexity deficiency to 0.05, and the LCD of the horizontal electric current density at the same region of Fig. 1 from frame 175 to 195. The arrows mark the centres of two merging magnetic flux tubes at the concentration of magnetic flux. The regions of intense LCD correspond to the interface boundary layers of two merging magnetic flux tubes.

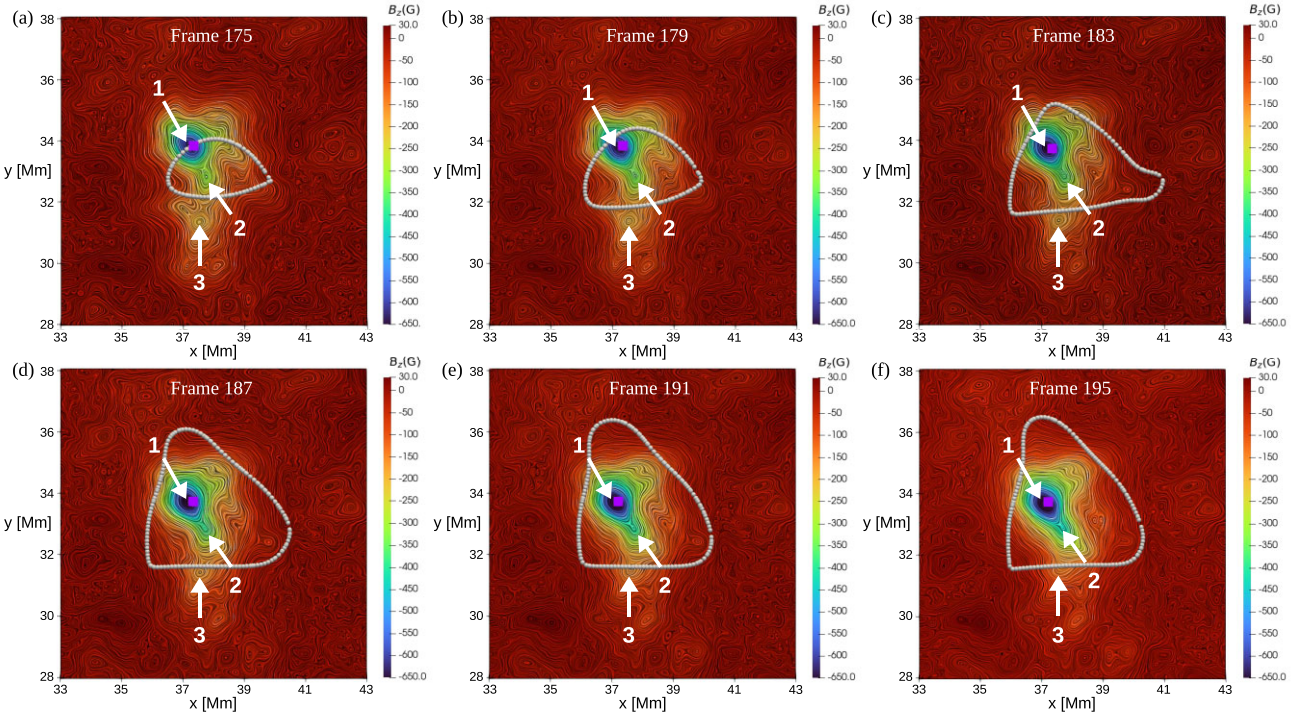

Figure 3. Spatiotemporal dynamics of the horizontal electric current density and line-of-sight magnetic field. The LIC-maps of the horizontal electric current density superposed by the line-of-sight magnetic field at the same region of Fig. 1. The grey circles denote the boundary of the persistent objective kinematic vortex from frame 175 to 195. The upper two arrows mark the centres of two merging magnetic flux tubes (1 and 2), and the vertical arrow at the bottom marks the centre of the third magnetic flux (3) which is not trapped by the vortex. The magenta squares denote the locations of the maxima of the line-of-sight magnetic field near the centre of the upper magnetic flux tube 1.

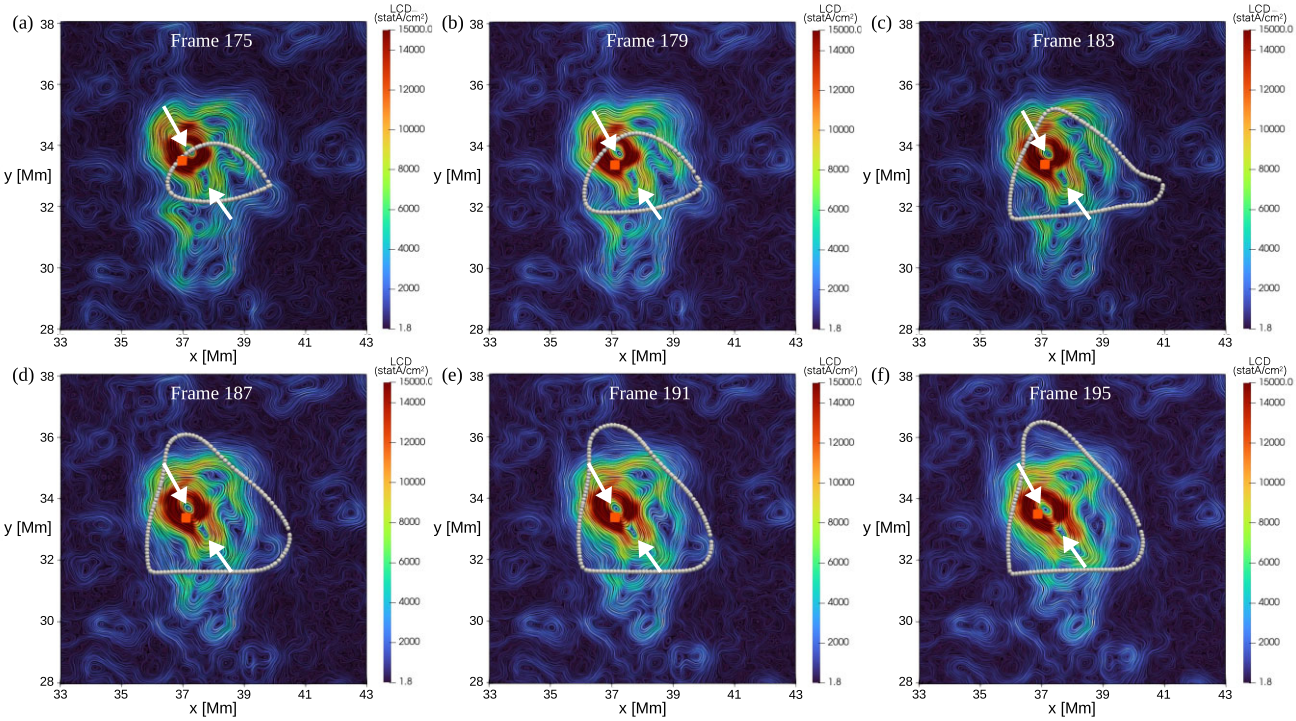

Figure 4. Spatiotemporal dynamics of the horizontal electric current density and LCD. The LIC-maps of the horizontal electric current density superposed by the LCD at the same region of Fig. 1. The grey circles denote the boundary of the persistent objective kinematic vortex from frame 175 to 195, and the arrows mark the centres of two merging magnetic flux tubes at the concentration of magnetic flux. The orange squares denote the locations of the maxima of LCD at the interface boundary layers of two merging magnetic flux tubes.

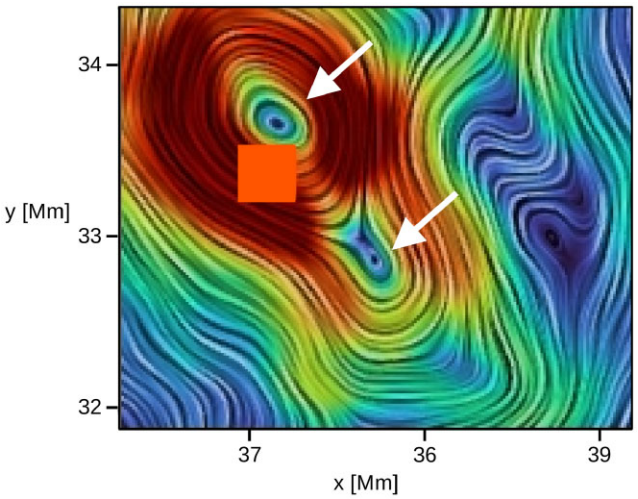

Figure 5. Maximum LCD at the interface boundary layers of merging magnetic flux tubes. Enlargement of the central region of Fig. 4(e) showing the location of LCD_{max} denoted by the orange square at the interface boundary layers of two merging magnetic flux tubes marked by two arrows.

tubes in Fig. 5 exhibit similar topology of the boundary layers of two merging magnetic vortices numerically simulated by Rempel et al. (2019; Fig. 8a), whereby the interface boundary layers of two merging magnetic flux tubes are given by a ridge of LCD situated between two magnetic flux tubes. Evidently, it follows from Fig. 5 that the maximum value of LCD_{max} denoted by the orange square is located at the interface boundary layers of two merging magnetic flux tubes.

Figs 6(a) and (b) show the temporal evolution of IVD at the centres of two (upper: tube 1, lower: tube 2) merging magnetic flux tubes indicated in Figs (2)–(5), respectively, and Fig. 6(c) shows the temporal evolution of IVD at the maximum of LCD_{max} at the interface boundary layers of two merging magnetic flux tubes. Fig. 6(d) shows the temporal evolution of the maximum of the LCD_{max} (interface) at the interface boundary layers, and Figs 6(e) and (f) show the temporal evolution of the modulus of the line-of-sight magnetic field $|B_{LOS}|$ at the centres of two merging magnetic flux tubes, respectively, where B_{LOS} has negative values. It follows from Figs 6(d) to (f) that during the vortex interval of 30 min under study the core magnetic fields and the interface electric current densities are intensified in the two merging magnetic flux tubes trapped by the vortex. Both tubes represent network structures so they interact frequently with the newly arriving magnetic patches from the interior of the supergranular cell. These newly arriving magnetic patches are coming from many directions. Hence, the electric current density can be intensified almost all the way around the network patches due to their interactions with those newly arriving magnetic fields. Since the LCD_{max} is mostly located on the left side of the upper tube, it is plausible that this maximum is at its position because of numerous magnetic cancellations involving opposite polarity internetwork fields that migrate towards the network and interact with network fields in that position. Figs 6(e) and (f) show that the intensification of magnetic field at the centres of magnetic flux tubes is monotonic, because the plasma flows there are dominated by the swirly motions towards the centres of magnetic flux tubes (i.e. the bathtub effect) which are co-spatial with the centre of vortical flows seen in Figs 1 and 2. The electric current density at the interface boundary layers is intensified monotonically initially, but exhibits small variations at the end of this interval because the boundary

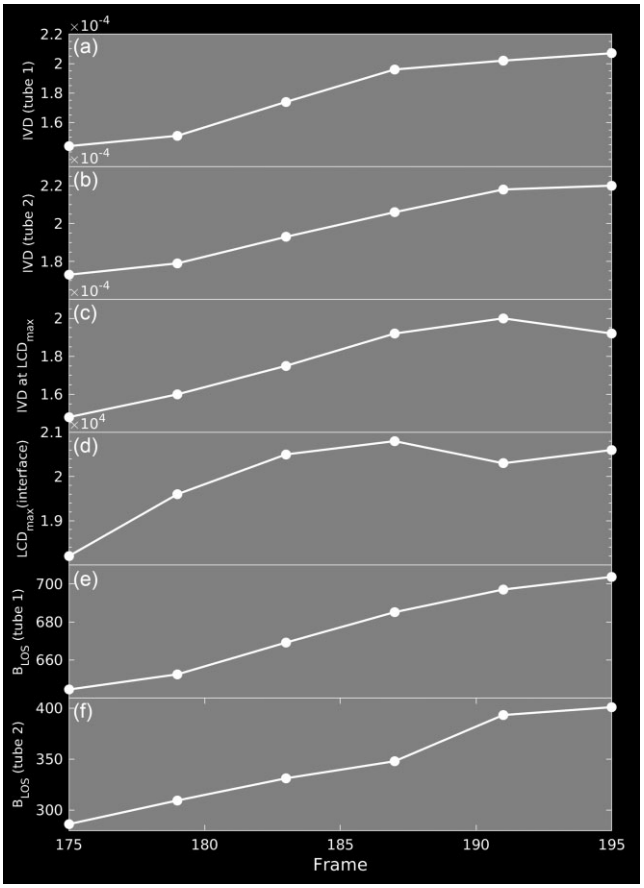

Figure 6. Intensification of magnetic fields at the centres and intensification of electric current densities at the interface boundary layers of two merging magnetic flux tubes. Temporal evolution from frame 175 to 195 of IVD in s^{-1} at the centre of upper (tube 1) merging magnetic flux tube (a) and lower (tube 2) magnetic flux tube (b); temporal evolution of IVD at the point of LCD_{max} (c) and the value of LCD_{max} in statampere cm^{-2} (d) at the interface boundary layers of two merging magnetic flux tubes; the modulus of line-of-sight magnetic field B_{LOS} in G at the centre of upper (tube 1) (e) and lower (tube 2) (f) merging magnetic flux tube.

layers of magnetic flux tubes become complex and inhomogeneous (Foullon et al. 2011).

In this section, we identify magnetic flux tubes visually from the closed contours of the LIC-maps of the horizontal electric current density. In Section 5, we will analyse the intensification of electromagnetic energy flux in the region of merging magnetic flux tubes. A precise detection of objective magnetic vortices can be carried out (see e.g. Silva et al. (2021)) using the technique of IACD developed by Rempel et al. (2017, 2019), but it requires knowledge of the horizontal magnetic field, which is not available in our data set.

4 STRETCHING-TWISTING-FOLDING LAGRANGIAN COHERENT STRUCTURES

The particle trajectories in turbulent flows in general exhibit Lagrangian chaos, with a defining property that the paths of initially neighbouring particles diverge exponentially when averaged over a given time interval, i.e. the finite-time Lyapunov exponent is positive. Batchelor (1950) was the first to show that the stretching action

of the turbulent velocity field leads to the intensification of the magnetic field strength. Moffatt & Proctor (1985) studied the stretch-twist-fold cycle capable of doubling the strength of a magnetic flux tube. Bajer & Moffatt (1990) demonstrated that stretch-twist-fold flows can become chaotic when the flow is dominated by its twist ingredient. A volume of passive scalar particles advected in a chaotic flow is stretched into a thin highly convoluted sheet as time progresses; such behaviour is conducive to strong mixing (Moffatt 2021).

Recently, the novel technique of Lagrangian coherent structures has been applied to elucidate Lagrangian chaos in solar and astrophysical plasma turbulence (Rempel, Chian & Brandenburg 2011; Yeates, Hornig & Welsch 2012; Chian et al. 2014, 2019, 2020; Rempel et al. 2017, 2019; Silva et al. 2018, 2020, 2021). In this paper, we showed that the area bounded by a supergranular persistent objective kinematic vortex linked to the rotational elliptic Lagrangian coherent structures, computed from the IVD by fixing the convexity deficiency parameter to 0.05, continuously enlarges due to chaotic stretching during the total time interval of 30 min seen in Figs 1–4. Table 1 lists the computed values of the temporal evolution of the vortex area which clearly provides the observational evidence of steady expansion of the supergranular vortex embedded in the photospheric magnetoconvective turbulence that leads to the amplification of magnetic fields at the cores and the intensification of electric current density at the interface boundary layers of two merging magnetic flux tubes trapped by the vortex. Numerical simulations of vortex have shown that a vortex is bounded by the hyperbolic attracting and repelling Lagrangian coherent structures associated with positive finite-time Lyapunov exponents (see Figs 1 and 4 of Rempel et al. 2017).

The Lagrangian centres and boundaries of solar supergranular cells are given by the local maximum of the forward and backward finite-time Lyapunov exponent, respectively (Chian et al. 2019, 2020), which are objective quantities (Haller 2015). The attracting Lagrangian coherent structures given by the backward finite-time Lyapunov exponent expose the location of the photospheric downflows and concentration of intense magnetic fields at supergranular junctions, whereas the repelling Lagrangian coherent structures (related to the quasi-separatrix layers (Yeates et al. 2012)) given by the forward finite-time Lyapunov exponent interconnect the Lagrangian centres of neighbouring supergranular cells. These topological hyperbolic Lagrangian transport barriers are found within a supergranular cell and from one magnetoconvective cell to other cells, which play a key role in the transport dynamics of network and internetwork magnetic elements. The intersections of attracting and repelling hyperbolic Lagrangian coherent structures form Lagrangian chaotic saddles, analogous to the non-attracting chaotic sets formed by the crossings of their stable and unstable manifolds in dynamical systems, which are responsible for chaotic transients and intermittency in turbulence (Rempel & Chian 2007; Chian et al. 2010; Rempel, Lesur & Proctor 2010; Chian, Muñoz & Rempel 2013).

Following Chian et al. (2020), we apply the ∼22 h *Hinode* data set used in this paper to detect Lagrangian chaotic saddles in the supergranular region under investigation. Fig. 7(a) shows the attracting LCS (i.e. the time-dependent unstable manifold) given by the lines of local maxima in the backward finite-time Lyapunov exponent field, computed for a grid of particles integrated from 19:25:29 UT on 2010 November 2 to 08:31:15 UT on 2010 November 2. Fig. 7(b) shows the repelling LCS (i.e. the time-dependent stable manifold), defined similarly, but from the forward finite-time Lyapunov exponent computed from 19:25:29 UT on 2010 November

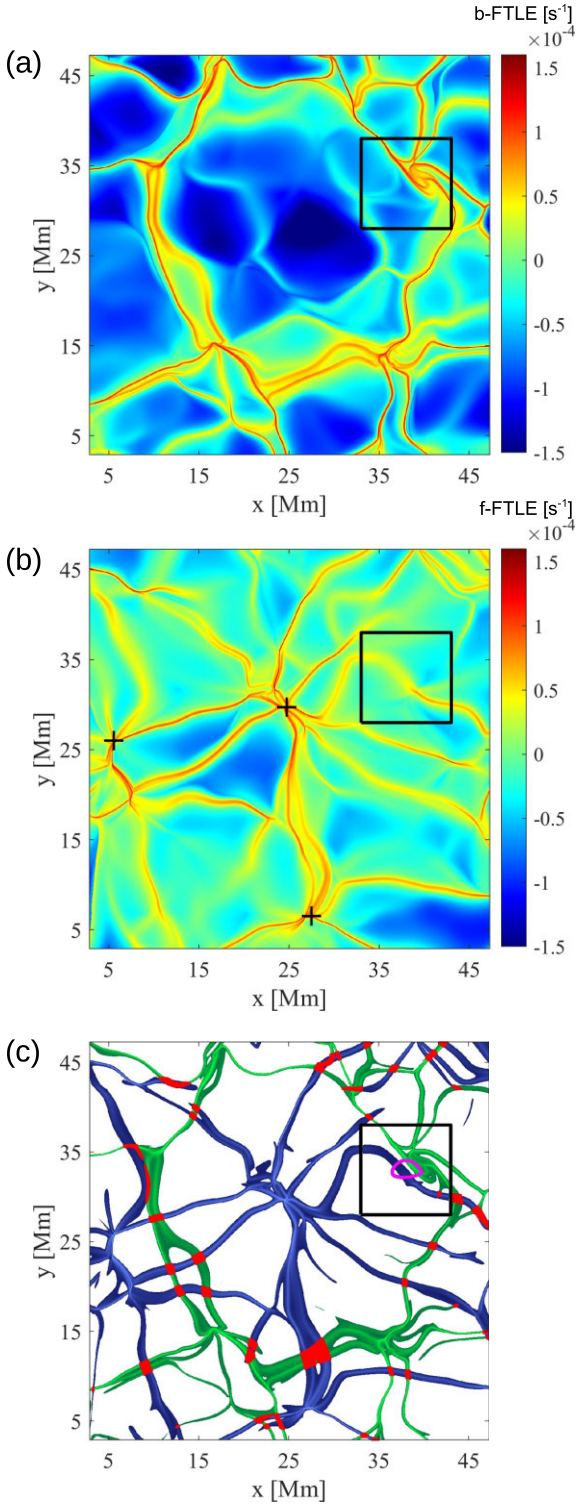

Figure 7. Lagrangian chaotic saddles and stretching-twisting-folding LCSs. (a) Attracting LCS given by b-FTLE computed from 19:25:29 UT on 2010 November 2 to 08:31:15 UT on 2010 November 2. (b) Repelling LCS given by the f-FTLE computed from 19:25:29 UT on 2010 November 2 to 06:19:42 UT on 2010 November 3. The black crosses mark the Lagrangian centres of supergranular cells. (c) Lagrangian chaotic saddles (red points) given by the intersections of the thresholded unstable (green) and stable (blue) manifolds with the threshold given by 0.3×10^{-4}, superposed by the boundary (magenta line) of the kinematic vortex computed by the LAVD for the time interval from 12:53:51 UT to 13:23:51 UT on 2010 November 2.

2 to 06:19:42 UT on 2010 November 3. Fig. 7(c) shows Lagrangian chaotic saddles (the set of red points) given by the intersections of the thresholded unstable and stable manifolds. The black box in Figs 7(a)–(c) corresponds to the region studied in Figs 1–6, superposed by the boundary of the persistent objective kinematic vortex computed by the LAVD from frame 175 to 195 on 2010 November 2. Evidently, the black box region of Figs 7(a) and (c) shows that unstable manifolds of Lagrangian chaotic saddles exhibit twisting and folding topological structures in the region of the persistent objective kinematic vortex and merging magnetic flux tubes, responsible for the intensification of magnetic fields and electric current densities. The identification of the twisting-folding patterns of the unstable manifolds is possible thanks to the long duration of ∼11 h *Hinode* data used to compute the backward finite-time Lyapunov exponent (Chian et al. 2020). Note from Fig. 7(c) that the persistent objective kinematic vortex, whose lifetime lies within the computed time interval of the unstable manifolds, is located in the gap region of Lagrangian chaotic saddles. The magnetic elements are advected by the photospheric flow radially outward from the centres of supergranular cells diverging preferentially along the ridges of the repelling Lagrangian coherent structures (Fig. 7b). At the Lagrangian chaotic saddle points (Fig. 7c) chaotic mixing occurs whereby the magnetic elements converge preferentially along the ridges of the attracting Lagrangian coherent structures (Fig. 7a). Eventually, the magnetic elements get trapped by the elliptic Lagrangian coherent structures (vortices) situated at the valleys of the repelling Lagrangian coherent structures and the ridges of the attracting Lagrangian coherent structures, which correspond to the regions of strong converging downflows responsible for convective collapse and intensification of magnetic field. It follows from Fig. 3 that initially (Fig. 3a) the two merging magnetic flux tubes are only partially trapped by the persistent kinematic vortex; as the vortex area expands they become almost fully trapped within the vortex boundary (Fig. 3f).

The supergranular vertex region inside the black box of Fig. 7 is dominated by strong kinematic and magnetic shears resulting from the complex interaction of converging plasma flows emanating from a number of neighboring supergranular cells. Fig. 7 shows that the finite-time stable and unstable manifolds computed for a long duration in this region do not intersect, thereby providing an extended region with gaps in Lagrangian chaotic saddles which facilitates the formation and interaction of persistent kinematic and magnetic vortices (Chian et al. 2020). It is worth noting that vortex stretching is a key feature of turbulent flows and is accompanied by vortex folding as a means of maintaining the energy of the vortex system constant, as in the case during the formation of the inertial range in turbulence (Chorin 1994; Kivotides & Leonard 2004). Our results of Table 1 and Fig. 7 render an observational support for this close link between vortex stretching and vortex folding in the photospheric turbulence. Elongated granular cells evolving from chaotic stretching are observed in conjunction with network magnetic flux tubes (Muller, Roudier & Hulot 1989) and emergence of solar magnetic fields (Gošić et al. 2021). As demonstrated by the numerical simulations of Yadav et al. (2020, 2021), a vortex observed by *Hinode* can be the product of the interaction of a number of vortices with smaller scales; it is likely that the persistent supergranular vortex studied in this paper is the consequence of the interaction of a number of short-lived intergranular vortices associated with elongated granular cells in a region of strong kinematic and magnetic shears. Hence, the steady expansion of vortex area seen in Table 1 and the steady increase of the IVD seen in Fig. 6 might be the manifestations of a steady chaotic stretching-twisting-folding of vortical flows driven by elongated granular cells resulting from deformation and intergranular vortex–vortex reconnections continuously generated by the intensification of supergranular turbulent downflows during this time interval. For example, the numerical simulations of Kivotides, Mee & Barenghi (2007) show that coherent structures can intensify magnetic fields consisted of twisted magnetic sheet structures that occasionally spiral around vortex filaments; most of the stretching of magnetic field lines takes place between vortex filaments caused by vortex–vortex reconnections which introduces a turbulent cascade of energy as a result of the rate of strain tensor.

5 INTENSIFICATION OF ELECTROMAGNETIC ENERGY FLUX AND MERGING OF MAGNETIC FLUX TUBES

Magnetic flux tubes are coherent structures that contain strong concentrations of magnetic fluxes and electromagnetic energy fluxes bounded by closed convex surfaces of electric current density as seen in Figs 3 and 4. The horizontal electric current density in Figs 3 and 4, computed from *Hinode*'s line-of-sight magnetic field by assuming vertically oriented magnetic fields, shows that the photosphere is permeated by a multitude of magnetic flux tubes, confirming the results of Giannattasio et al. (2020) and Gošić et al. (2021). In this section, we show that the identification of magnetic flux tubes in the supergranular vortical region of Figs 3 and 4 and the detailed spatiotemporal dynamics of merging of magnetic flux tubes can be elucidated by calculating the horizontal Poynting vector.

The electromagnetic energy flux given by the Poynting vector (S) can be written in MHD approximation as (Silva et al. 2022)

$$S = \frac{1}{4\pi}\mathbf{B} \times (\mathbf{u} \times \mathbf{B}). \tag{7}$$

A realistic Bifrost simulation of a quiet-Sun demonstrated that the total electromagnetic energy flux in the photosphere occurs mainly parallel to the photosphere, concentrating in small regions along the intergranular lanes (Silva et al. 2022). This finding was validated by *SUNRISE/IMaX* data. Hence, Silva et al. (2022) proposed a proxy for the horizontal electromagnetic energy flux:

$$S \sim \frac{1}{4\pi} u_h {B_z}^2, \tag{8}$$

where u_h is the modulus of the horizontal plasma velocity and B_z is the longitudinal magnetic field.

Fig. 8 shows a time sequence of the computed horizontal electromagnetic energy flux from the *Hinode* data superposed by the LIC-maps of the horizontal plasma velocity and the same vortex boundaries of Figs 1–4 from frame 175 to 195. Evidently, Fig. 8 identifies three patches of concentration of electromagnetic energy flux; each patch is situated at the same location occupied by one of three magnetic flux tubes detected in Fig. 3. As is well known, in general the magnetic field intensity of the majority of magnetic flux tubes in the internetwork region is weak, but the magnetic field intensity of magnetic flux tubes in the supergranular junctions can reach kiloGauss range owing to strong shears related to strong downdrafts. This is consistent with the results of Fig. 8, which shows that the electromagnetic energy flux is weak in the internetwork region but strong in the region of supergranular vortical flows, albeit these results are obtained from equation (8), which is less accurate in regions outside the intergranular lanes and supergranular junctions. The spatiotemporal dynamics of the merging process involving magnetic flux tubes 1 and 2 seen in Figs 3 is well depicted in Fig. 8. In the beginning of this 30-min interval, the top two patches of concentration of electromagnetic energy flux are weakly connected,

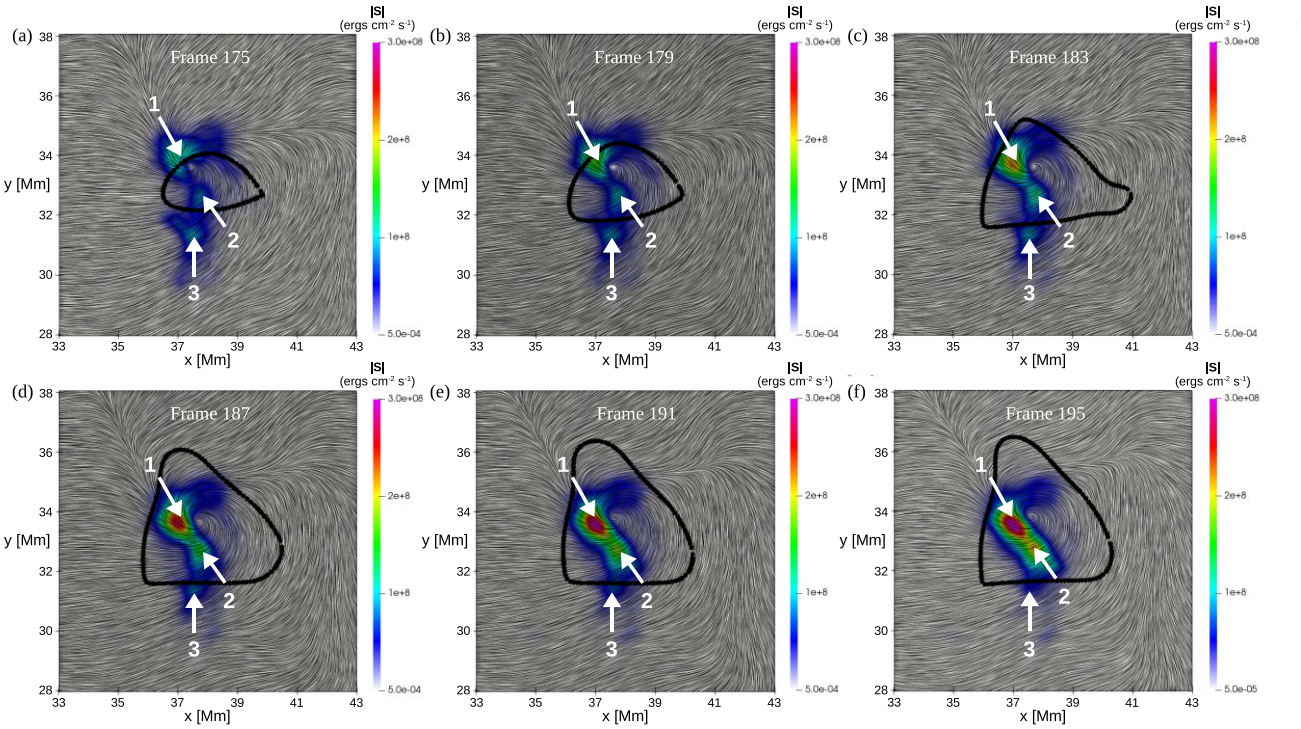

Figure 8. Spatiotemporal dynamics of the horizontal electromagnetic energy flux. The LIC-maps of horizontal photospheric velocity fields superposed by the boundary (black circles) of the persistent objective kinematic vortex computed by the IVD by fixing the value of convexity deficiency to 0.05, and the horizontal electromagnetic energy flux at the same region of Figs 1–4 from frame 175 to 195. The upper two arrows mark the centres of two merging magnetic flux tubes (1 and 2), and the vertical arrow at the bottom marks the centre of the third magnetic flux tube (3) which is not trapped by the vortex.

as seen in Fig. 8(a). It follows from the sequence of images in Fig. 8 that a steady vortical expansion leads to a steady merging of the top two patches, accompanied by a steady intensification of electromagnetic energy flux in both patches, as demonstrated in the temporal evolution of the electromagnetic energy flux at the centres of magnetic flux tubes 1 and 2 given in Table 2. At the end of this time interval, two initially irregularly shaped and weakly connected patches seen in Fig. 8(a) turn into a single elongated regularly shaped and strongly connected coherent electromagnetic structure as the result of tube-tube merging seen in Fig. 8(f). Hence, the steady chaotic stretching of supergranular vortex is able to drive a self-organized restructuring of electromagnetic energy flux, which undergoes a pattern transition from a regime of complexity (incoherence) to a regime of simplicity (coherence).

A comparison of the images of magnetic flux (Fig. 1) with the images of the horizontal electromagnetic energy flux (Fig. 8) shows that while it is not possible to detect three magnetic flux tubes individually in the images of Fig. 1, which only plots B_z, it becomes possible in the images of Fig. 8, which plots $\frac{1}{4\pi} u_h {B_z}^2$. This indicates that the horizontal electromagnetic energy flux given by equation (8) provides an effective method of detecting magnetic flux tubes in conjunction with the LIC-maps of the horizontal electric current density (Fig. 3) in the photospheric region of intense magnetic flux concentrations.

The persistent kinematic vortex plays a key role in acting as a transport barrier for trapping magnetic flux tubes 1 and 2 in the merging process, seen in Figs 2–5 and 8. In contrast, a gradual decay of the intensity of electromagnetic energy flux is observed in the bottom third patch of concentration of electromagnetic energy flux in Fig. 8, situated at the same location occupied by the magnetic flux tube 3 in Fig. 3, as seen in the temporal evolution of $|S|$ at the centre of tube 3 given in Table 2. Fig. 8 shows that during the 30-min time interval the bottom third patch is not trapped by the vortex, since it is located outside the vortex boundary, thus, it is excluded from the merging process. The images of the spatiotemporal dynamics of the horizontal electromagnetic energy flux in Fig. 8 provide a clearer view for the evolution of tube-tube merging process identified in Figs 3 and 4.

6 DISCUSSION AND CONCLUSIONS

The interaction between turbulent convection and magnetic field is fundamental for understanding the formation and evolution of magnetic field, electric current density, and electromagnetic energy flux in the solar photosphere and atmosphere. A previous work by Requerey et al. (2018) on the temporal evolution of vorticity, Dopplergram, and magnetic flux density in the same supergranular vertex region studied in this paper showed that vorticity plays a crucial role in intensifying and stabilizing the network magnetic element, supporting the theory of Schüssler (1984). In this paper, we carry out an in-depth investigation of the magnetic field-vortex relation in the supergranular turbulence. By computing the horizontal electric current density from the line-of-sight magnetic field and the horizontal electromagnetic energy flux, we were able to detect two kG magnetic flux tubes undergoing merging in the network region of a persistent objective kinematic vortex, as seen in Figs 2–5 and 8. In particular, we obtained observational evidence of the intensification of magnetic field, electric current density, and electromagnetic energy flux in merging magnetic flux tubes driven by supergranular vortical flows, as seen in Fig. 6 and Table 2. Our findings also suggest that the

Table 2. Temporal evolution of the modulus of horizontal electromagnetic energy flux at the centres of three magnetic flux tubes in the region of supergranular vortical flows from frame 175 to frame 195 on 2010 November 2.

Frame number	175	179	183	187	191	195
$\|S\|$(tube 1) in erg cm^{-2} s^{-1}	5.77×10^7	1.07×10^8	1.68×10^8	2.18×10^8	2.54×10^8	2.64×10^8
$\|S\|$(tube 2) in erg cm^{-2} s^{-1}	7.31×10^7	8.667×10^7	1.09×10^8	1.38×10^8	1.77×10^8	2.12×10^8
$\|S\|$(tube 3) in erg cm^{-2} s^{-1}	9.44×10^7	9.28×10^7	9.27×10^7	8.16×10^7	7.17×10^7	5.5×10^7

vorticity in the region of merging magnetic flux tubes, indicated by the values of IVD, tends to increase as the magnetic field intensifies, as seen in Fig. 6. This is in accordance with the findings of Shelyag et al. (2012) and Cuissa & Steiner (2020), which showed that the magnetic fields play a key role on the evolution of vorticity.

The stretching-twisting-folding dynamics is always expected in chaotic flows, but it is not a simple task to find observational evidence of chaos in spacecraft data. We were able to show in Sections 2–5 that a 2D study based on spacecraft observation of intensity continuum and line-of-sight magnetogram is capable of providing some relevant insights of the vorticity-magnetic field relation in solar photosphere. In particular, our results based on the computation of the IVD were able to obtain a clear observational evidence of expansion of vortex area in chaotic vortical flows in Figs 1–4, Fig. 8, and Table 1; and our investigations based on the computation of finite-time Lyapunov exponents were able to obtain a clear observational evidence of Lagrangian chaos, Lagrangian chaotic saddles, and stretching-twisting-folding topology of chaotic vortical flows in Fig. 7. Vortex stretching is the elongation (expansion) of vortices in fluid flows associated with a corresponding increase of the component of vorticity in the stretching direction due to the conservation of angular momentum, given by the $\omega \cdot \nabla \mathbf{u}$ source term in the vorticity equation, where ω is the vorticity and $\mathbf{u}$ is the fluid velocity (Porter, Jones & Ryu 2015). Stretching is a manifestation of deformation induced by the Cauchy-Green strain-rate tensor related to the velocity gradient; it amplifies the vorticity when the velocity is diverging in the direction parallel to the vorticity. Vortex stretching accounts for the formation of large-scale vortices resulting from the interaction of small-scale vortices via turbulence energy cascade in atmosphere (Luo & Liu 2008), ocean (Marez et al. 2020), and protoplanetary discs (Tarczay-Nehéz, Regály & Vorobyov 2020).

The non-linear dynamics of turbulence in fluids and plasmas is governed by hyperbolic and elliptic Lagrangian coherent structures. Hyperbolic LCS are responsible for deformation and advective mixing over finite-time intervals; elliptic LCS are vortex cores that inhibit mixing. Repelling hyperbolic LCS are the stretching material lines that split up fluid blobs; attracting hyperbolic LCS are the folding material lines that attract and then elongate fluid blobs, causing stretching (Haller 2001). The repelling material lines act as finite-time stable manifolds for the trajectory, while the attracting material lines act as finite-time unstable manifolds. The exponential rate of repulsion (attraction) is determined by the forward (backward) finite-time Lyapunov exponent, respectively, given by the local maximum eigenvalues of the Cauchy–Green deformation tensor. Particles spend a long time near stretching lines; in particular, particles close to stretching lines tend to accumulate near folding lines and then spiral into a vortical region of a nearby elliptic LCS. Hence, the spatiotemporal dynamics of elliptic LCS is closely related to hyperbolic LCS. In this paper, we reported space plasma observation of vortex stretching manifested by a steady increase of the area of the objective kinematic vortex in the supergranular turbulence shown in Table 1. This steady increase of vortex area is accompanied by a steady increase of vorticity (IVD), seen in Figs 6(a)–(c), which serves as a signature of steady increase of stretching of stable and unstable manifolds in the region outside the vortex boundary, driven by a steady increase of velocity shear, which leads to an intensification of intergranular vortex-vortex interactions associated with elongated granulations. Our results are supported by recent LCS studies of vortex-vortex interactions in laboratory experiments and numerical simulations (Qin, Liu & Xiang 2018; Zheng et al. 2021).

Intensification of magnetic field by merger of magnetic elements has been detected recently by observations and numerical simulations, which show that two magnetic bright points move towards each other before merging with the magnetic field rising and peaking as they coalesce (Keys et al. 2020). During the interval studied in this paper, signatures of merging involving two magnetic flux tubes in the region of an expanding persistent objective kinematic vortex are seen in Figs 2–5 and 8, which suggest that the intensification of core magnetic fields, core electromagnetic energy fluxes, and interface electric current densities can, to some extent, be attributed to the merging of two magnetic flux tubes trapped in the interior of the persistent objective kinematic vortex. It is possible that the electric currents are not generated solely by the two merging network magnetic features, since they may also be partially generated by cancellation events between the network and internetwork magnetic patches that occur frequently over 24-h continuous *Hinode* observation of this photospheric region (Gošić et al. 2014).

It is worth pointing out that the sites of tube-tube merging can occur either in the photosphere or in the chromosphere-upper solar atmosphere. The horizontal electric current density swirls, seen in Figs 3–5, correspond to the photospheric footpoints of magnetic flux tubes. Gošić et al. (2021, 2022) showed that magnetic loops can emerge from their footpoints in the photosphere and rise up through the solar atmosphere to reach the chromospheric heights. Magnetic flux tubes undergo a considerable expansion when they reach the upper solar atmosphere, which facilitates their interactions with the nearby magnetic flux tubes even though their footpoints in the photosphere are not adjacent to each other. Moreover, the photospheric vortical motions can induce complex topology of braided coronal magnetic fields that may lead to magnetic reconnection and heating on a timescale of hours, as shown by Candelaresi et al. (2018). In that sense, a major result of this paper given in Table 2 is the intensification of the core electromagnetic energy flux in merging magnetic flux tubes. Due to the vortical motions, a net upward Poynting flux might be generated as the vortical flows perturb the magnetic field lines, but unfortunately our analysis was limited to the horizontal Poynting flux as we only have the line-of-sight magnetic field component.

We have shown in a series of papers that Lagrangian coherent structures provide a powerful tool to unravel the complex nature of supergranular turbulence in active and quiet Sun. In Chian et al. (2014), we established the correspondence of the high network magnetic flux concentrations to the ridges of attracting Lagrangian coherent structures, and demonstrated that the boundaries of supergranular cells are given by the maxima of the backward finite-time

Lypapunov exponent of the horizontal plasma velocity, which expose the location of the sinks of photospheric flows at supergranular junctions in a plage region of AR 10930. In Chian et al. (2019), we showed that the centre of a supergranular cell is given by the local maximum of forward finite-time Lyapunov exponent and the repelling Lagrangian coherent structures interconnect the Lagrangian centres of neighbouring supergranular cells in the quiet Sun. In Chian et al. (2020), we presented observational evidence of Lagrangian chaotic saddles in plasmas given by the intersections of finite-time unstable and stable manifolds, and showed that the persistent objective vortices are formed in the gap regions of Lagrangian chaotic saddles at supergranular junctions in the quiet Sun.

In this paper, we reported the observational evidence of chaotic stretching-twisting-folding of Lagrangian coherent structures in photospheric turbulent vortical flows at a quiet-Sun supergranular junction that leads to the intensification of core magnetic field and interface electric current density in two merging magnetic flux tubes trapped by a persistent objective kinematic vortex. Furthermore, we report for the first time a solar observation of the intensification of electromagnetic energy flux driven by this merger of magnetic flux tubes. Our novel approach can be applied to the study of turbulent dynamo in solar plasmas (Xu et al. 2020) and magnetic reconnection of merging magnetic flux tubes (Gekelman et al. 2022). Recent advances in computational techniques to improve the spatiotemporal resolution of reconstructed spacecraft images using deep learning algorithms (Asensio, Requerey & Vitas 2017; Tremblay et al. 2021; Ishikawa et al. 2022) and to inpaint spacecraft images of highly corrupted data (Rempel et al. 2022) can be used in conjunction with the methodology developed in this paper to probe the complex spatiotemporal dynamics and structures of astrophysical and laboratory plasmas.

ACKNOWLEDGEMENTS

This work is dedicated to Professor George Batchelor for his pioneer work on the intensification of magnetic field by a turbulent vortical flow and founding of the Department of Applied Mathematics and Theoretical Physics at the University of Cambridge and Journal of Fluid Mechanics. The data used here were acquired in the framework of the Hinode Operation Plan 151 'Flux replacement in the solar network and internetwork'. We thank the Hinode Chief Observers for the efforts they made to accommodate our demanding observations. Hinode is a Japanese mission developed and launched by ISAS/JAXA, with NAOJ as a domestic partner and NASA and STFC (UK) as international partners. Financial support by the State Agency for Research of the Spanish Ministerio de Ciencia e Innovación through grant RTI2018-096886-B-C5 (including FEDER funds) and through a Center of Excellence Severo Ochoa award to Instituto de Astrofísica de Andalucía (SEV-2017-0709) is gratefully acknowledged. SSAS is grateful to Science and Technology Facilities Council (STFC) grant ST/V000977/1, and The Royal Society, International Exchanges Scheme, collaboration with Brazil (IES191114). MG was supported by NASA contract NNM07AA01C (Solar-B (Hinode) Focal Plane Package Phase E). ELR acknowledges Brazilian agency CNPq (Grant 306920/2020-4) for the financial support.

DATA AVAILABILITY

The data underlying this article will be shared on reasonable request to the corresponding author.

REFERENCES

Asensio Ramos A., Requerey I. S., Vitas N., 2017, A&A, 596, A15
Attie R., Innes D. E., Potts H. E., 2009, A&A, 493, L13
Attie R., Innes D. E., Solanki S. K., Glassmeier K. H., 2016, A&A, 596, A15
Bajer K., Moffatt H. K., 1990, J. Fluid Mech., 212, 337
Bale S. D. et al., 2021, ApJ, 923, 174
Balmaceda L., Vargas Domínguez S., Palacios J., Cabello I., Domingo V, 2010, A&A, 513, L6
Batchelor G. K., 1950, Proc. R. Soc. London, A201, 405
Battaglia A. F., Cuissa J. R. C., Calvo F., Bossart A. A., Steiner O., 2021, A&A, 649, A121
Bellot Rubio L., Orozco Suárez D., 2019, Living Rev. Sol. Phys., 16, 1
Bellot Rubio L. R., Rodríguez Hidalgo I., Collados M., Khomenko E., Ruiz Cobo B., 2001, ApJ, 560, 1010
Brandt P. N., Scharmert G. B., Ferguson S., Shine R. A., Tarbell T. D., Title A. M., 1988, Nature, 335, 238
Candelaresi S., Pontin D. I., Yeates A. R., Bushby P. J., Hornig G., 2018, ApJ, 864, 157
Chian A. C. L., Miranda R. A., Rempel E. L., Saiki Y., Yamada M., 2010, Phys. Rev. Lett., 104, 254102
Chian A. C. L., Muñoz P. R., Rempel E. L., 2013, Phys. Rev. E, 88, 052910
Chian A. C.-L., Rempel E. L., Aulanier G., Schmieder B., Shadden S. C., Welsch B. T., Yeates A. R., 2014, ApJ, 786, 51
Chian A. C.-L., Silva S. S. A., Rempel E. L., Gošić M., Bellot Rubio L. R., Kusano K., Miranda R. A., Requerey I. S., 2019, MNRAS, 488, 3076
Chian A. C.-L., Silva S. S. A., Rempel E. L., Bellot Rubio L. R., Gošić M., Kusano K., Park S. H., 2020, Phys. Rev. E, 102, 060201(R)
Chorin A. J., 1994, Vorticity and Turbulence. Springer, New York
Cuissa J. R. C., Steiner O., 2020, A&A, 639, A118
Fargette N. et al., 2021, ApJ, 919, 96
Foullon C., Verwichte E., Nakariakov V. M., Nykyri K., Farrugia C. J., 2011, ApJ, 729, L8
Gekelman W., Tanga S. W., DeHaas T., Vincena S., Pribyl P., Sydora R., 2022, PNAS, 116, 18239
Giannattasio F., Consolini G., Berrilli F., Del Moro D., 2020, ApJ, 904, 7
Gošić M., Bello Rubio L., Orozco Suarez D., Katsukawa Y., Del Toro Iniesta J. C., 2014, ApJ, 797, 49
Gošić M., De Pontieu B., Bellot Rubio L. R., Sainz Dalda A. S., Esteban Pozuelo S., 2021, ApJ, 911, 41
Gošić M., Bello Rubio L., Cheung M. C. M., Orozco Suarez D. O., Katsukawa Y., Del Toro Iniesta J. C., 2022, ApJ, 925, 188
Haller G., 2001, Phys. Fluids, 13, 3365
Haller G., 2015, Annu. Rev. Fluid Mech., 47, 137
Haller G., Hadjighasem A., Farazmand M., Huhn F., 2016, J. Fluid Mech., 795, 136
Hewitt R. L., Shelyag S., Mathioudakis M., Keenan F. P., 2014, A&A, 565, A84
Innes D. E., Genetelli A., Attie R., Potts H. E., 2009, A&A, 495, 319
Ishikawa R. T., Nakata M., Yukio Katsukawa Y., Masada Y., Riethmüller T. L., 2022, A&A, 658, A142
Keys P. H. et al., 2020, A&A, 633, A60
Kitiashvili I. N., Kosovichev A. G., Mansour N. N., Wray A. A., 2012, ApJ, 751, L21
Kitiashvili I. N., Kosovichev A. G., Lele S. K., Mansour N. N., Wray A. A., 2013, ApJ, 770, 37
Kitiashvili I. N., Kosovichev A. G., Mansour N. N., Wray A. A., 2015, ApJ, 809, 84
Kivotides D, Leonard A., 2004, Europhys. Lett., 66, 69
Kivotides D., Mee A. J., Barenghi C. F., 2007, New J. Phys., 9, 291
Luo Z., Liu C., 2008, Meteorol. Atmos. Phys., 99, 65
Marez C., Carton X., L'Hégaret P., Meunier T., Stegner A., Le Vu B., Morvan M., 2020, Sci. Rep. 10, 2897
Martínez-Sykora J., Hansteen V. H., Gudiksen B., Carlsson M., De Pontieu B., Gošić M., 2019, ApJ, 878, 40
Moffatt H. K., 2021, J. Fluid Mech., 914, P1
Moffatt H. K., Proctor M. R. E., 1985, J. Fluid Mech., 154, 493
Muller R., Roudier T., Hulot J. C., 1989, Solar Phys. 119, 229

Nagata S. et al., 2008, ApJ, 677, L145
Parker E. N., 1978, ApJ, 221, 368
Porter D. H., Jones T. W., Ryu D., 2015, ApJ, 810, 93
Qin S., Liu H., Xiang Y., 2018, Phys. Fluids, 30, 011901
Rempel E. L., Chian A. C. L., 2007, Phys. Rev. Lett., 98, 014101
Rempel E. L., Lesur G., Proctor M. R. E., 2010, Phys. Rev. Lett., 105, 044501
Rempel E. L., Chian A. C.-L., Brandenburg A., 2011, ApJ, 735, L9
Rempel E. L., Chian A. C.-L., Beron-Vera F. J., Haller G., Szanyi S., 2017, MNRAS, 466, L108
Rempel E. L., Gomes T. F. P., Silva S. S. A., Chian A. C.-L., 2019, Phys. Rev E, 99, 043206
Rempel E. L., Chertovskih R., Davletshina K. R., Silva S. S. A., Welsch B. T., Chian A. C.-L., 2022, ApJ, 933, 2
Requerey I. S., Del Toro Iniesta J. C., Bellot Rubio L. R., Martínez Pillet V., Solanki S. K., Schmidt W., 2015, ApJ, 810, 79
Requerey I. S., Cobo B. R., Gov sić M., Bellot Rubio L. R., 2018, A&A, 610, A84
Roudier T., Švanda M., Malherbe J. M., Ballot J., Korda D., Frank Z., 2021, A&A, 647, A178
Schüssler M., 1984, A&A, 140, 453
Shelyag S., Mathioudakis M., Keenan F. P., 2012, ApJ, 753, L22
Silva S. S. A., Rempel E. L., Gomes T. F. P., Requerey I. S., Chian A. C.-L., 2018, ApJ, 863, L2
Silva S. S. A., Fedun V., Verth G., Rempel E. L., Shelyag S., 2020, ApJ, 898, 137
Silva S. S. A., Verth G., Rempel E. L., Shelyag S., Schiavo L. A. C. A., Fedun V., 2021, ApJ, 915, 24
Silva S. S. A., Murabito M., Jafarzadeh S., Stangliani M., Verth G., Ballai I., Fedun V., 2022, ApJ, 927, 146
Spruit H. C., 1979, Solar Phys., 61, 363
Tarczay-Nehéz D., Regály Zs., Vorobyov E., 2020, MNRAS, 493, 3014
Tremblay B., Cossette J.-F., Kazachenko M. D., Charbonneau P., Vincent A., 2021, J. Space Weather Space Clim., 11, 9
Vargas Domínguez S., Palacios J., Balmaceda L., Cabello I., Doming V., 2015, Solar Phys., 290, 301
Xu Z., Ji H., Ji K., Bi Y., Yang B., Hong J., Yang J., 2020, ApJ, 900, L17
Yadav N., Cameron R. H., Solanki S. K., 2020, ApJ, 894, L17
Yadav N., Cameron R. H., Solanki S. K., 2021, A&A, 645, A3
Yang B., Jiang Y., Yang J., Hong J., Xu Z., 2015, ApJ, 803, 86
Yeates A. R., Hornig G., Welsch B. T., 2012, A&A, 539, A1
Zheng Z., Fan Z., Wang Z., Yu B., Zhang B., He M., 2021, J. Vis., 24, 19

This paper has been typeset from a TEX/LATEX file prepared by the author.